Acta Astronautica 205 (2023) 33–46

Contents lists available at ScienceDirect

Acta Astronautica

journal homepage: www.elsevier.com/locate/actaastro

Research paper

Rendezvous and proximity operations design of an active debris removal service to a large constellation fleet

Giacomo Borelli *, Gabriella Gaias, Camilla Colombo

Politecnico di Milano, 20156, Milano, Italy

ARTICLE INFO

Keywords:
Active debris removal
Large constellations
Proximity operations
GNC
Contactless detumbling

ABSTRACT

This work presents the design of rendezvous and close proximity operations for an active debris removal service for maintenance and disposal of a large constellation fleet. The design drivers of the service are safety and robustness of the operations, capability to remove a satellite under every condition, and high level of autonomy to reduce the service-related operations' cost. Accordingly, the most challenging case of a rendezvous with a uncooperative non-collaborative target satellite is considered and a strategy to reduce its rotational motion is also presented. As for the rendezvous, the focus is on the relative trajectory design. First a guidance solution capable to maximise the observability property of the angles-only relative navigation problem is developed. Second, a set of convenient relative trajectories to enable target inspection for various illumination conditions is selected and an approach to ensure safe transitions among them is settled. Both these designed strategies can be readily implemented on autonomous spaceborne systems. Simulations are run for two constellation fleets, differing in mass of the single s/c and orbit's altitude and inclination.

1. Introduction

In recent years, the launch activities in Low Earth Orbit (LEO) are rapidly increasing the number of objects in orbit. The implementation and deployment of large constellations to provide broad-band global internet coverage from space have overcome any other launch activities in terms of number of satellites [1]. The sustainability of this fast evolving orbital system needs to be addressed by private and public institutions to avoid the congestion of the space environment in the future. A set of guidelines issued by the Inter-Agency Space Debris Co-ordination Committee were produced to limit the uncontrolled growth of space debris and prevent the triggering of a *point of no return* referred as to the Kessler syndrome [2].

It is envisioned that large constellations providers need to have a responsible behaviour both to allow a safe operation of the constellation satellites and to avoid endangering other parties' assets in orbit. Considering that the number of satellites deployed within one single constellation in LEO is planned to be in the order of thousands, the probability of contingencies and failures of some of the assets will affect the operations within the congested orbital region.

Several studies in literature have highlighted the impact of failures and limited Post Mission Disposal (PMD) success rate on the debris object population in LEO. In [3] the authors showed the different evolution of the debris environment in function of different success of the passive mitigation strategies after the introduction of a representative constellation of 1080 satellites deployed in LEO at 1100 km of altitude. Even though the increase of the number of objects can be mitigated by ensuring a high post mission disposal success rate, the trend in the long term growth will anyway increase. Radtke et al. [4] analysed that for the case study of the OneWeb constellation (first generation) there is a 35% of probability of creating fragments in orbit during the constellation mission lifetime. Refs. [5–9] discuss the effects of constellation traffic in the LEO environment evaluating the debris evolution in function of the post mission disposal success rate and estimating the future number of collisions. In NASA study [10], a success rate of 99% is estimated to be required to limit the growth of debris in such regions. Such high PMD success rate for constellations satellites it is likely not to occur in the future.

A combination of passive and active mitigation techniques is therefore envisioned in the future to control the growth of debris in congested LEO region. In this work, the remediation strategy of Active Debris Removal (ADR) is considered as service for large constellations assets in the crowded orbital slots regions. Other than the benefit of the removal of failed objects of the constellation, the implementation of such service would additionally foster fleet preservation and management by performing In-Orbit Servicing (IOS) tasks when necessary. Servicing mission to large constellations assets have recently been considered by the community. Generally, a mission architecture capable

* Corresponding author.
E-mail address: giacomo.borelli@polimi.it (G. Borelli).

https://doi.org/10.1016/j.actaastro.2023.01.021
Received 18 October 2022; Accepted 12 January 2023
Available online 20 January 2023

of performing multiple removal/servicing within the same mission is considered to guarantee financial feasibility [11–15].

In addition to the mission financial feasibility, several technical challenges are still present in the implementation of each deorbit/servicing task. Particularly, the Rendezvous and Proximity Operations (RPOs) to an uncooperative and non-collaborative target represent the most critical part of the service implementation and are the subject study of this work. In the scenario where targets at different in-orbit conditions require servicing, the importance of a robust, safe and systematic design is paramount. In the past studies, the proximity operations design for approaching uncooperative and non-collaborative objects usually focuses in the target properties and the monitoring of its conditions at mission design level before launch [16,17]. One notable example is the ESA e.Deorbit study which extensively studied the status of the target ENVISAT with several observation campaigns to characterise its conditions, particularly concerning the rotational behaviour in orbit [18].

In the case of large constellations assets, these practices will be limited both by: (1) the poor visibility from ground of the failed satellites conditions with ground sensors, (2) the need of removing all the target failed satellites regardless their status and eventually adapt during the mission operations. Moreover, given the repeatability required for these complex operations, the safety, flexibility and robustness of the design are key for their successful implementation. In addition, the autonomy level of the servicer performing these tasks in orbit is considered important to reduce the cost of ground support during the mission operations.

The technical aspects involved in proximity operations have been widely addressed by the scientific community in the last decades, starting from the far approach phases up to the target docking and stabilisation. The proximity operations design up to the target capture and de-orbiting have been studied multiple programs [19–21]. However, the approaches taken in these works are strongly dependent on the target characteristics and status, which influence the capture method selection and proximity operations design.

The key issues tackled in this work are the one related to the limited knowledge of the target status prior capture whose solutions will enable a flexible and robust implementation of an ADR service for large constellations fleets. Particularly, the focus is placed on the trajectory and operations design in the phases starting from first target in-orbit acquisition up to close operations to prepare the target for safe capture. The Concept of Operations (ConOps) considered is based on the strong heritage of past missions and studies, with implementations of some novelties which guarantee in each phase the fulfilment of the specific design drivers of the service.

In the far-range phase, different approaches for trajectory design are explored in literature. Approaches to cooperative targets benefit from a strong heritage coming from the Automated Transfer Vehicle (ATV) missions [22] and the Orbital Express and Engineering Test Satellite No. 7 (ETS-VII) demonstration missions [23,24]. Generally, the v-bar approach is adopted to reduce the separation and rendezvous with the target. Nonetheless, when dealing with the uncooperative targets, the level of safety of the v-bar approach is typically not satisfactory. Spiralling approaches using the relative Eccentricity and Inclination (E/I) vector separation [25] have been considered thanks to the inherent independence on the along-track component of the navigation solution. This aspect guarantees the safety, in terms of target-servicer collision avoidance, of the trajectory. Such approach have been firstly demonstrated in-orbit to approach an uncooperative object during the AVANTI experiment [26]. The Restore-L servicing mission also will use the spiralling approach at closer separation while still relying on a co-elliptic far-range approach to semi-cooperative LandSat 7 target [27]. In light of the advantages in relative navigation and safety, the drift spiralling approach is employed here, introducing the novelty of enhancing the Angles-Only (AO) navigation system performance during the approach directly at the guidance level. Differently from previous formulations where the observability gain is evaluated considering the manoeuvre actions on the relative trajectory [28,29], here a formulation of the enhanced observability between two ROE states along the trajectory is introduced. Specifically, this formulation allows an analytic solution of the guidance in ROE space considering delta-v equivalent costs and a penalty on the observability enhancement. This aspect is considered instrumental for the autonomous implementation of the guidance onboard with a solution capable of increasing the robustness of the navigation solution.

The ROE space is exploited also in the inspection phase starting from few hundreds meters of separation [30,31]. The Walking Safety Ellipse (WSE) approach applied in literature uses spiralling trajectory to fly-around the target with the aim of observing its features. The geometric and analytic design of WSE sequence of trajectory is also exploited in this work, with two improvements that are aimed at increasing the efficiency and the safety of the trajectory. Namely the phasing angle of the relative eccentricity and inclination vectors is changed during the sequence in order have the servicer sensors' boresight in more suitable illumination condition. Moreover, the impulsive transfer between the WSE sequence is approached by enforcing the passive safety also along the transfer trajectory and not only at the boundary conditions of WSE. In such a way, the safety for autonomous operations is greatly aided.

At last, the inclusion of a contactless control phase for the target tumbling motion is discussed. This phase is considered key to the successful close approach and capture of fast tumbling target. Studies in literature have explored the contactless control of an uncooperative object though different methods [32–35]. In this work, a contactless control using the plume impingement is explored [36–39], demonstrating the feasibility of reducing the target residual angular momentum magnitude with the on-board thrusters of the servicer spacecraft.

The work described in this paper was part of a phase 0/A design of an ADR service technology under the ESA/OneWeb funded Sunrise programme. The effort was taken by a consortium led by D-Orbit S.p.a. and Politecnico di Milano. Following this introduction, the paper presents a brief description of the service mission concept under study Section 2. Subsequently, the RPO ConOps designed is presented together with the ADR payload selected for the service mission in Section 3. The core part of the work lies in the following sections, where the RPO phases strategies and design are presented and discussed, namely the far to mid range rendezvous (Section 4), the inspection phase (Section 5) and concluding with the phase of debris target preparation before rigid capture (Section 6). Finally, the conclusions and future developments are discussed.

2. Service mission concept overview

Different mission architectures for an end-of-life servicing and removal service for large constellations satellites have been explored in recent studies. Authors in [11,12] consider different possible mission architectures within a mission analysis trade-off for the removal service of multiple targets. The possible mission architectures and strategies are hereafter mentioned with the aim of highlighting the implications of the overall mission architecture on the rendezvous and proximity operations design.

Robotic capture is considered within these mission architectures. The repeatability and reliability of this capture method is particularly suited for the capture of multiple target withing the same mission.

One of the mission architectures explored in [11,12] considers a servicer (chaser) satellite which approaches, captures and de-orbits sequentially all the failed constellation satellites. Here the servicer will transfer itself with the target attached to a disposal orbit which will guarantee a reentry time of at least five years. To increase the number of removable objects by one single servicer, a refuelling station is also explored as an alternative option. As third option, the use of de-orbiting kits to attach to the failed satellites is studied to allow propellant saving

Table 1
Baseline constellation platforms taken as reference in the study for ADR service.

	Light Target (LT)	Heavy Target (HT)
Platform	Arrow platform (OneWeb)	EliTeBus-1000 (GLOBALSTAR)
Mass [kg]	150	750
Altitude [km]	1200	1400
Inclination [deg]	87.9	52

Table 2
ADR payload sensors employed for the proximity operations.

Sensor	r_{max} [km]	FOV [deg]	Mass [kg]	Power [W]
VIS NFOV	50	6–12	1	5
VIS WFOV	10	40–60	1	5
Flash LiDAR	1	15–30	5	50
IR camera	3	12–40	2	10

by assigning the task of transfer to the disposal orbit to a stand-alone detachable subsystem.

Other than the different robotic operations required once the target has been captured, i.e. stack de-orbiting or kit attachment, the complexities of the RPOs before capture are shared by of all the architectures considered. Namely the uncooperativeness and non-collaborative nature of the target to be rigidly capture with the servicer spacecraft.

3. Proximity concept of operations

In this work two different baseline constellation targets are considered, with the characteristics shown in Table 1. The reference targets are selected as representative of constellation platforms, including small class satellite (light target) and large class satellite (heavy target). The main high-level requirement in the definition of the proximity ConOps and in the approach strategies include the capability of rendezvous and capture with the uncooperative and non-collaborative target regardless the illumination or rotational conditions. To support the whole set of proximity operations, the servicer is equipped with a sensor suite comprehending the sensors shown in Table 2 which provide the required redundancy and robustness of the navigation subsystem during all the phases. Table 2 shows maximum operating distance r_{max}, Field of View (FOV), mass and power properties of the sensors. Two cameras in the visible spectrum are used with two different Field Of View (FOV) to cope with varying separations with the target. An Infrared (IR) imager is also envisioned to provide measurements acquisition during harsh illumination conditions. At last, a flash LiDar is envisioned to provide also the range information at closer separations.

Autonomy, safety and robustness of operations are considered two key drivers in the RPO design within the ADR service. Particularly, the capability of ensuring the deorbiting of every failed satellite is considered instrumental to the mission success. The proximity ConOps envisioned is shown in Fig. 1. The sequence of operations during one approach in chronological order during the mission timeline are: (1) absolute orbit phasing, (2) far-range rendezvous, (3) mid-range rendezvous, (4) inspection, (5) target preparation for robotic capture, (6) final approach motion, (7) robotic capture operations, (8) stack stabilisation and deorbiting.

After a coarse orbit phasing managed by the absolute Attitude and Orbit Control System (AOCS) of the servicer, the proximity operations will start as soon as the target can be detected by the on-board relative sensors. The mean separation between servicer and target to begin the relative operations is considered at around 40 km based on the results of [26,40] . After the detection of the target and the commissioning of on-board systems applicable to the approach phase (i.e., relative sensors), the servicer will begin to reduce the mean separation with the target using the Relative Guidance Navigation and Control (R-GNC) exploiting an impulsive manoeuvres strategy. The spiralling trajectory approach towards the target characterised by passive safety is adopted with AO navigation solution using Line of Sight (LOS) measurements taken with the on-board cameras. At closer separations starting from 1 km to few hundreds meters, the mid-range rendezvous begins where different sensors' data will complement the AO navigation solution to ensure the required accuracy for the subsequent closer operations.

From few hundred meters of separation, the inspection phase will start with the aim of activation and verification of the sensor for close range navigation and estimation of the target physical and dynamical state. In this phase, the attitude motion and target's features will be estimated and its entity will drive the selection of the subsequent sequence of operations. In fact, in the cases where the tumbling rate of the target does not allow the safe approach and synchronisation with the predefined capture point, the servicer will start the operations to prepare the target for the rigid capture. More specifically, the operations of contactless damping of the tumbling rates using the servicer thrusters plumes is used to drive the target rotation rates below the safe threshold for synchronisation [39]. Once the target is in a condition to be captured, the forced motion synchronisation profile is performed to bring the servicer to the capture hold point and to perform the robotic capture operations. On the other hand, when the target is not tumbling at unmanageable rates, the forced motion to synchronise the spacecraft platform towards the capturing point is performed without prior additional operations. At the capture hold point, the robotic operations will take place. These consists in the control of the manipulator and servicer system to capture the target. After the securing of the capture and stabilising the stack, the servicer will de-orbit the target by transferring the stack to the disposal orbit. In the next sections, the design strategies adopted in this work starting from the far range rendezvous up to the phase of target preparation for rigid capture are described.

4. Far and mid-range rendezvous design

Two Line Elements (TLE) data are available for each known target and can be used to support acquisition phase [41]. However, the uncertainties associated with TLE data are too large to reliably use this information to bring the servicer to a closer rendezvous with the target [42,43], especially in the plane perpendicular to the orbital velocity [41,42,44]. Therefore, the servicer will need to rely on the relative on-board sensors to support relative navigation tasks. Note that reducing the need of costly and frequent ground segment observations, link and support.

After the detection of the target in the camera field of view at approximately around 40 km, the Relative Guidance Navigation and Control (R-GNC) drives the reduction of the separation with the target progressively and autonomously.

4.1. Relative guidance and control approach

The guidance and control solution are based on the framework originally introduced by Gaias et al. [26,45,46], which uses impulsive manoeuvres to reconfigure the relative orbit between two satellites on a near circular LEO orbit. The general idea of this framework is to decouple the Guidance and Control (GC) solutions with the aim of obtaining a computationally efficient algorithm suitable for an on-board implementation. This framework uses a quasi-non singular ROEs parametrisation, which is defined as function of the Keplerian elements of the servicer $(\cdot)_s$ and target $(\cdot)_t$ satellites [47]. The non-dimensional ROEs are expressed as follows:

$$\delta\boldsymbol{\alpha} = \begin{bmatrix} \delta a \\ \delta\lambda \\ \delta e_x \\ \delta e_y \\ \delta i_x \\ \delta i_y \end{bmatrix} = \begin{bmatrix} (a_s - a_t)/a_s \\ u_s - u_t + (\Omega_s - \Omega_t)\cos in_s \\ e_s \cos\omega_s - e_t \cos\omega_t \\ e_s \sin\omega_s - e_t \sin\omega_t \\ in_s - in_t \\ (\Omega_s - \Omega_t)\sin in_s \end{bmatrix} \tag{1}$$

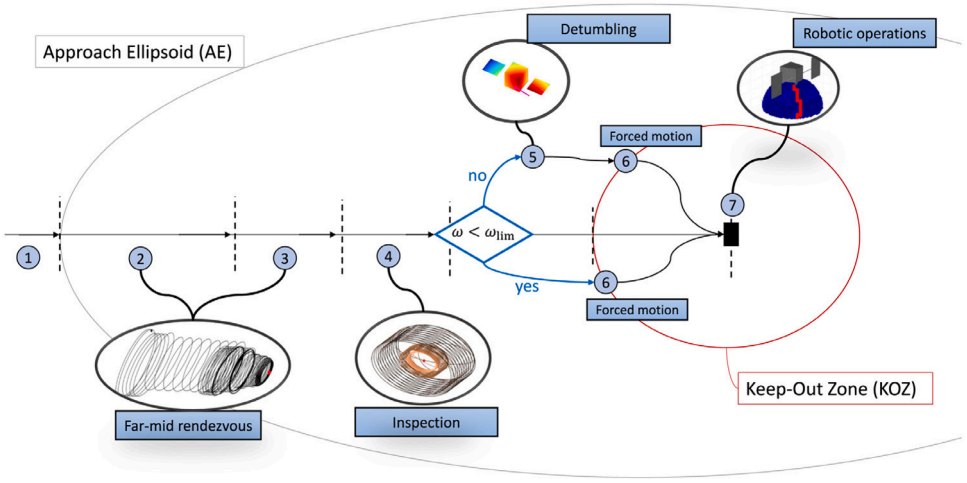

Fig. 1. Proximity of operations concept of operation scheme.

The Keplerian elements of the servicer and target orbits used in the formulation of Eq. (1) are the semi-major axis a, eccentricity e, inclination in, right ascension of ascending node Ω, argument of perigee ω and argument of latitude u expressed in the Earth centred equatorial frame. Assuming the target on a near-circular orbit, the relative motion dynamics solution formulated in ROE and subject to K impulsive manoeuvres at times $t_{k,i}$ can be expressed as:

$$(a\delta\boldsymbol{\alpha}_f) = \boldsymbol{\Phi}_{0,f}(a\delta\boldsymbol{\alpha}_0) + \boldsymbol{\Phi}_{1,f}\mathrm{B}_1\delta\boldsymbol{v}_1 + \cdots + \boldsymbol{\Phi}_{K,f}\mathrm{B}_K\delta\boldsymbol{v}_K \tag{2}$$

where $a\delta\boldsymbol{\alpha}$ is the ROE state vector, $\boldsymbol{\Phi}_{i,j}$ is the State Transition Matrix (STM) from time t_i to time t_j, and $\boldsymbol{B}_i$ is the control input matrix obtained from the Gauss Variational Equations (GVE) at time t_i shown in Eq. (3) [47,48].

$$\boldsymbol{B} = \frac{1}{n}\begin{bmatrix} 0 & 2 & 0 \\ -2 & 0 & 0 \\ \sin(u) & 2\cos(u) & 0 \\ -\cos(u) & 2\sin(u) & \cos(u) \\ 0 & 0 & \sin(u) \end{bmatrix} \tag{3}$$

In this work, the STM reported in Eq. (4) includes the secular J_2 effects on the relative motion dynamics, while the drag effects introduced by Gaias et al. [48] are neglected due to the limited influence on the motion at the high altitude of the constellations reported in Table 1 taken as a baseline.

$$\boldsymbol{\Phi}(t_0,t) = \begin{bmatrix} 1 & 0 & 0 & 0 & 0 & 0 \\ (\nu+\mu_A)(t-t_0) & 1 & 0 & 0 & (\mu_I)(t-t_0) & 0 \\ 0 & 0 & \cos(\dot{\varphi}(t-t_0)) & -\sin(\dot{\varphi}(t-t_0)) & 0 & 0 \\ 0 & 0 & \sin(\dot{\varphi}(t-t_0)) & \cos(\dot{\varphi}(t-t_0)) & 0 & 0 \\ 0 & 0 & 0 & 0 & 1 & 0 \\ \lambda_A(t-t_0) & 0 & 0 & 0 & \lambda_I(t-t_0) & 1 \end{bmatrix} \tag{4}$$

The coefficients introduced depend on the J_2 parameters and chief orbit parameters, for more detail the reader is referred to Gaias et al. [26,48].

The adopted guidance strategy seeks for the solution of Eq. (2) considering directly the relative dynamics evolution in the ROE space, instead of solving for the impulses δv_k. The impulses definition problem to follow the specified trajectory in the ROE space will then be solved separately. The solution of the guidance problem relies on discretising the trajectory in the ROE space in m predefined time nodes, and solving the required $\Delta\delta\boldsymbol{\alpha}_i$ ROE jumps required to reach the final state $\delta\boldsymbol{\alpha}_f$ and to minimise a cost function associated with trajectory cost and properties. By doing so, the final state $\delta\boldsymbol{\alpha}_f$ considering the ROE impulsive jumps in the elements space can be expressed linearly as function of the ROE jumps:

$$a\delta\boldsymbol{\alpha}_f = \boldsymbol{\Phi}_{0,f}a\delta\boldsymbol{\alpha}_0 + \boldsymbol{\Phi}_{1,f}a\Delta\delta\boldsymbol{\alpha}_1 + \cdots + \boldsymbol{\Phi}_{M,f}a\Delta\delta\boldsymbol{\alpha}_M \tag{5}$$

Considering the reconfiguration Eq. (5) in the ROE space, the final state constraints $a\delta\boldsymbol{\alpha}(t_f) = a\delta\boldsymbol{\alpha}_f$ can be directly enforced considering the last ROE jump $a\Delta\delta\boldsymbol{\alpha}_M$ in function of the previous $M-1$ jumps.

$$\begin{aligned} a\Delta\delta\boldsymbol{\alpha}_M = \boldsymbol{\Phi}_{M,f}^{-1}\big(a\delta\boldsymbol{\alpha}_f - \big(\boldsymbol{\Phi}_{0,f}a\delta\boldsymbol{\alpha}_0 + \boldsymbol{\Phi}_{1,f}a\Delta\delta\boldsymbol{\alpha}_1 + \cdots \\ +\boldsymbol{\Phi}_{M-1,f}a\Delta\delta\boldsymbol{\alpha}_{M-1}\big)\big) \end{aligned} \tag{6}$$

The $M-1$ ROE jumps $a\Delta\delta\boldsymbol{\alpha}_i$ are then compactly rearranged in the following vector:

$$\boldsymbol{x} = [a\Delta\delta\boldsymbol{\alpha}_1, a\Delta\delta\boldsymbol{\alpha}_2, \ldots, a\Delta\delta\boldsymbol{\alpha}_{m-1}]^{\mathrm{T}} \tag{7}$$

The cost function considered in this work J is built upon the cost function J_e introduced in [46], which considers the quadratic contributions of the forced impulsive ROE jumps at times t_i. The minimum-path cost function J_e is defined as follows [46]:

$$J_e = \sum_i^M (a\Delta\delta a)_i^2 + + \sum_i^M (a\Delta\delta\lambda)_i^2 + \sum_i^M \|a\Delta\delta\boldsymbol{e}\|_i^2 + \sum_i^M \|a\Delta\delta\boldsymbol{i}\|_i^2 \tag{8}$$

where $a\Delta\delta\boldsymbol{e}$ and $a\Delta\delta\boldsymbol{i}$ represent the eccentricity and inclination vector jumps respectively. In the ROE space, the J_e can be defined as the measure of the path spanned during the reconfiguration. Minimising the J_e is then equivalent to minimise the square of the delta-v, in the cases where only tangential and normal burns are used (which is a necessary condition to achieve delta-v optimal reconfigurations [45]).

Including the dependency of the final M forced ROE jump to the previous $M-1$ shown in Eq. (6), the cost function J_e can be written as:

$$J_e = \boldsymbol{x}^{\mathrm{T}}\boldsymbol{x} + (\mathrm{P} + \mathrm{H}\boldsymbol{x})^{\mathrm{T}}(\mathrm{P} + \mathrm{H}\boldsymbol{x}) \tag{9}$$

with

$$\mathrm{P} = \boldsymbol{\Phi}_{M,f}^{-1}[a\delta\boldsymbol{\alpha}_f - \boldsymbol{\Phi}_{0,f}a\delta\boldsymbol{\alpha}_0] \tag{10}$$

$$\mathrm{H} = -\boldsymbol{\Phi}_{M,f}^{-1}[\boldsymbol{\Phi}_{1,f} \quad , \quad \boldsymbol{\Phi}_{2,f} \quad , \quad \ldots \quad , \quad \boldsymbol{\Phi}_{M-1,f}] \tag{11}$$

and with the $\boldsymbol{x}$ vector that now contains only the $M-1$ ROE jumps.

The novel addition of this work is a penalty factor to quantify and therefore improve the observability of the relative trajectory in the angles-only navigation regime. As a result the cost function J introduced in this work is expressed as the sum of a delta-v optimal contribution of J_e with the observability penalty function J_o, weighted appropriately by the weight w:

$$J = J_e + wJ_o \tag{12}$$

The idea of the present guidance solution is that, provided that the J cost function is a quadratic convex form in $\boldsymbol{x}$ (as the one used to represent the delta-v contribution J_e), the solution can be obtained simply solving a linear system analytically. This property allows an analytic solution of the guidance problem which is particularly suitable for on-board implementation in the contest of autonomous operations. In fact, if the latter condition holds the necessary conditions for the minimisation of J can be written as an unconstrained problem as follows:

$$\frac{\partial J}{\partial \boldsymbol{x}^{\mathrm{T}}} = \mathbf{0}_{(m-1\times 1)} \tag{13}$$

The novel contribution of this work in this regard is the incorporation of penalty term J_o in the cost function for the ROE based guidance. The penalty term is introduced in a quadratic form in function of the $\boldsymbol{X}$ ROE jumps, hence retaining the analytic solution of the guidance problem. The J_o penalty serves as an index of the degree of observability of a certain ROE sequence. In fact, as it will be explained in detail in the next sub-section, to approach the target from large separations the servicer will make use of the AO navigation strategy. The natural relative orbits perturbed by the J_2 effect are observable considering only bearing measurements. Nonetheless, the errors in the line of sight measurements provide the system with very weak observability in practice. Forced manoeuvres acting on the relative trajectory will improve the degree of observability of the system by applying a known perturbation. In literature, several observability definitions for the angles-only problem can be found, particularly in presence of manoeuvres [28,29,49,50]. The definition of J_o stems from the positive linear independence condition between the relative position vector at time t_q under the influence of the forced ROE trajectory $\delta x^F(t_q)$ and the relative position vector at time t_q subject only to the natural relative motion evolution $\delta x^N(t_q)$ from time t_{q-1} [29,50]. The latter condition can be written as:

$$\alpha\left(\delta \boldsymbol{x}^N(t_q)\right)^{\mathrm{T}} \neq \left(\delta \boldsymbol{x}^F(t_q)\right) \quad \text{with} \quad \alpha > 0, \quad \alpha \in \mathbb{R} \tag{14}$$

The relative position vectors $\delta \boldsymbol{x}$ are considered in the Radial Transversal Normal (RTN) reference frame, that for near-circular orbit features the first axis along the radial direction of the target position vector, the second axis towards the velocity vector and the third axis along the target orbit specific angular momentum vector.

The observability enhancement for a certain ROE state relative to the time span (t_{q-1}, t_q) is obtained by minimising the following dot product:

$$J_{o,q} = \left(\Gamma\left(t_q\right)\delta\boldsymbol{\alpha}_q^N\right)^T\left(\Gamma\left(t_q\right)\delta\boldsymbol{\alpha}_q^F\right) \tag{15}$$

where the minimum conditions correspond to anti-parallel position vectors $\delta \boldsymbol{x}$. In this expression, to quantify the improvement of observability of a certain ROE state at time t_q after the actions in the segment starting from t_{q-1}, the position vectors in Eq. (14) is considered only at one argument of latitude $u_q \in (0, 2\pi)$. A more complete representation of the discrepancy of natural and forced ROE trajectory in terms of bearing evolution along a ROE state can be achieved considering more argument of latitudes $u_q = nt_q$. In the latter case, the size of the problem will increase. The transformation map from the cartesian position vector in RTN frame to the relative orbital element state at time t_q is [51]:

$$\Gamma(t_q) = \begin{bmatrix} 1 & 0 & -\cos(nt_q) & -\sin(nt_q) & 0 & 0 \\ 0 & 1 & 2\sin(nt_q) & -2\cos(nt_q) & 0 & 0 \\ 0 & 0 & 0 & 0 & \sin(nt_q) & \cos(nt_q) \end{bmatrix} \tag{16}$$

where n is the mean motion. The errors introduced by such first order mapping from ROE to rectilinear Cartesian coordinates in far range have been assessed to not affect the observability enhancement formulations in terms of LOS vectors discrepancy. In order to map the observability enhancement obtained from a certain trajectory in the ROE space, the observability nodes are considered coincident with the guidance nodes $t_q = t_i$. The full observability penalty function J_o reduces then to the sum of the penalty functions for the whole set of observability enhanced nodes $q = 1, \ldots, Q$.

$$J_o = \sum_{q=1}^{Q} w_q\left(\Gamma\left(t_q\right)\delta\boldsymbol{\alpha}_q^N\right)^T\left(\Gamma\left(t_q\right)\delta\boldsymbol{\alpha}_q^F\right) \tag{17}$$

Expanding in Eq. (15) the dependency of the ROE vector at time t_q with the ROE jump vector $\boldsymbol{x}$, the resulting expression can be expressed as:

$$\begin{aligned} J_{o,q} &= \left[\Gamma(t_q)\boldsymbol{\Phi}_{q-1,q}\delta\boldsymbol{\alpha}_{q-1}\right]^{\mathrm{T}}\left[\Gamma(t_q)\left(\boldsymbol{\Phi}_{0,t_q}\delta\boldsymbol{\alpha}_0 + \left[\boldsymbol{\Phi}_{q,0}, \boldsymbol{\Phi}_{q,1}, \cdots, \boldsymbol{\Phi}_{q,q-1} \quad I\right]\boldsymbol{x}_q\right)\right] \\ &= \left[\Gamma(t_q)\boldsymbol{\Phi}_{q-1,q}\left(\boldsymbol{\Phi}_{0,q-1}\delta\boldsymbol{\alpha}_0 + \mathrm{D}_{q-1}\mathrm{C}_{q-1}\boldsymbol{x}\right)\right]^{\mathrm{T}}\left[\Gamma(t_q)\left(\boldsymbol{\Phi}_{0,q}\delta\boldsymbol{\alpha}_0 + \mathrm{D}_q\mathrm{C}_q\boldsymbol{x}\right)\right] \end{aligned}$$

where

$$\mathrm{D}_{q-1} = \left[\boldsymbol{\Phi}_{1,q}, \boldsymbol{\Phi}_{2,q}, \cdots, \boldsymbol{\Phi}_{q-1,q}\right] \tag{18}$$

$$\mathrm{D}_q = \left[\boldsymbol{\Phi}_{1,q}, \boldsymbol{\Phi}_{2,q}, \cdots, \boldsymbol{\Phi}_{q-1,q}, \mathrm{I}_{(6\times 6)}\right] \tag{19}$$

$$\mathrm{C}_q = \left[\begin{array}{ccc|ccc} 1 & & 0 & 0 & & 0 \\ & \ddots & & & \ddots & \\ 0 & & 1 & 0 & & 0 \end{array}\right]$$

where the C_q matrix is composed by an identity matrix of size $(q \times q)$ and a zeros matrix of size $(q \times (M-q))$ such that $\boldsymbol{x}_q = C_q\boldsymbol{x}$. Rearranging the matrices in Eqs. (17) separating the contributions of quadratic and linear contributions with respect to $\boldsymbol{x}$, the observability penalty is expressed as:

$$J_o = \sum_{q}^{Q} w_q\left(\boldsymbol{x}^{\mathrm{T}}\mathrm{L}_{1,q} + \boldsymbol{x}^{\mathrm{T}}\mathrm{L}_{2,q}\boldsymbol{x}\right) \tag{20}$$

Finally, including the derived expression in Eq. (12), the cost function J reduces to a quadratic function in function of the ROE jumps vector $\boldsymbol{x}$ and the predefined weights w_q. The necessary condition for the minimisation of J reduces now to evaluating the stationary point of its first variation.

$$\frac{\partial J}{\partial \boldsymbol{x}} = \left(\mathrm{G}_{tot}\right)\boldsymbol{x} + \mathrm{D}_{tot} = 0 \tag{21}$$

where

$$\mathrm{G}_{tot} = \mathrm{I} + \mathrm{H}^{\mathrm{T}}\mathrm{H} + \sum_{q}^{Q} w_q L_{2,q} \tag{22}$$

$$\mathrm{D}_{tot} = \mathrm{P} + \sum_{q}^{Q} w_q L_{1,q} \tag{23}$$

The solution of the linear system of Eq. (21) provides the analytic guidance solution in the ROE jumps space $\boldsymbol{x}$. To retain meaningful and feasible analytic solutions of the guidance problem in ROE space, the observability weights w_q are important for the convexity of the quadratic function J and have to be defined with care. Particularly, in this work the weights are defined as follows:

$$w_q = \frac{J_e^{only} k_{obs,q}}{\delta\lambda_{e,q}^2 N_Q} \tag{24}$$

where J_e^{only} and $\delta\lambda_{e,j}$ are respectively the minimum path cost function value and the relative longitude that come from the solution without the observability enhancement, pre-computed solving the minimum path only problem analytically with $w_q = 0$. The weights contribution due to relative longitude of the energy optimal solution is introduced to realistically compare the dot product of Eq. (15) with the angular difference between the two line of sight vectors, assuming their length equal to the relative longitude magnitude. The constant values $k_{obs,q}$ are user defined constants for each observability enhanced node to tune the influence of observability enhancement over the minimum-path energy optimal contribution. At last, the value N_Q is the

number of observability nodes considered in the overall reconfiguration discretisation.

Once the guidance trajectory in the ROE space is solved, the ROE jump vector sequence $\boldsymbol{x}$ and the configuration guidance times grid is provided to the local control function, which is in charge of planning and placing impulsive $\delta \boldsymbol{v}_k$ manoeuvres to track the guidance trajectory in the ROE space. The method to place the manoeuvres inside an intermediate configuration guidance time space (t_{i-1}, t_i) is based on the analytic optimal impulsive scheme described in [26,45] and is here briefly explained. The reconfiguration problem between $\delta \boldsymbol{\alpha}_i$ and $\delta \boldsymbol{\alpha}_{i-1}$, with impulsive manoeuvres, can be expressed as:

$$\begin{bmatrix} \boldsymbol{\Phi}_{i,1}\mathrm{B}_1 & \dots & \boldsymbol{\Phi}_{i,k}\mathrm{B}_K \end{bmatrix} \begin{bmatrix} \delta \boldsymbol{v}_1 \\ \vdots \\ \delta \boldsymbol{v}_K \end{bmatrix} = \left(\delta \boldsymbol{\alpha}_i - \boldsymbol{\Phi}_{i-1,i} \delta \boldsymbol{\alpha}_{i-1} \right) = \boldsymbol{x}_i \tag{25}$$

where $\delta \boldsymbol{v}_k = [\delta v_{R,k}, \delta v_{T,k}, \delta v_{N,k}]$ is the impulsive delta-v at time t_k. The scheme adopted considers the in-plane and out-of-plane problem decoupled from one another. The effects of J_2 in the local manoeuvres placement is neglected due to the short reconfiguration period considered in the local control problem. Moreover, the iterative application of the scheme recomputing the guidance solutions, which consider the J_2 effects, over the whole approach avoids the building up of the errors due to this assumption. Particularly, the in-plane reconfiguration problem is solved using three tangential manoeuvres placed at the argument of latitudes defined as:

$$u_{ip,k} = \tan^{-1}\left(\frac{\Delta \delta e_y}{\Delta \delta e_x} \right) + n_{man,k}\ \pi, \quad n_{man,k} \in \mathbb{N}, \quad n_{man,k} \geq 0 \tag{26}$$

with $n_{man,k}$ selected as positive integers ensuring that the last manoeuvre δv_K will be placed before the next guidance time node t_i. The out-of-plane reconfiguration control problem is solved placing one manoeuvre at the argument of latitude computed as:

$$u_{oop,k} = \tan^{-1}\left(\frac{\Delta \delta i_y}{\Delta \delta i_x} \right) \tag{27}$$

More details on the control scheme assumptions and optimality can be found in [45].

4.2. Relative navigation approach

During the far and mid range phases, a key function of the R-GNC autonomous operations is the relative navigation function. From far range, the use of a visible camera providing bearing only measurements restricts the adoption of an angles-only navigation strategy acquiring bearing measurements of the target with the servicer on-board sensors [40,42,44]. The relative navigation filter is implemented as an Extended Kalman Filter (EKF) whose task is to estimate directly the ROE state. The approach adopted has been demonstrated to be suitable for spaceborne implementation [40,44].

The model of the system dynamics implemented in the filter exploits the state transition matrix of the J_2 perturbed relative motion reported in Eq. (4) [48]. The AO navigation is then performed filtering the bearing measurements (azimuth and elevation) of the target in the camera frame. At closer range, the measurement of range from the active LiDAR sensor will complement the measurement filtered by the EKF routine resulting in a substantial improvement of the navigation solution. The impulsive manoeuvres are added to the filter without manoeuvre execution errors. The process noise covariance is set as $\mathrm{diag}([10^{-4}, 0.03, 0.03, 0.03, 0.03, 0.01])$ meters. The filter initialisation is done considering the target state knowledge from the TLE data, with along track uncertainties of one kilometers and 100 meters in radial and cross track. The mapping between the LOS vector and the ROE state used is the one reported in Eq. (16). The sensors parameters selected for the analysis and simulations are reported in Table 3, where the sensors noise correspond to the noise used in the filter parameters. The measurements rates reported in Table 3 refer to the phases of far and mid-range rendezvous. The LiDAR is considered functioning only four times per revolution in mid-range. Though a more substantial use in the inspection and close approach sequence is envisioned.

Table 3
Sensors' parameters used in the navigation system.

Sensor	Parameter	Value
VIS camera	Noise	80 arcsec
	Rate	0.033 Hz
Flash LiDAR	Noise	50 cm
	Rate	$6 \cdot 10^{-4}$ Hz

Table 4
Far and mid range rendezvous phases considered in the simulation campaign. The Angles + Range (A+R) navigation solution correspond to the simultaneous use of bearing and range measurements.

Phase	Guid.	Nav.	$a\delta\boldsymbol{\alpha}$ [km]	ΔT [Periods]
Far-range 1	$J_e + J_o$	AO	$a\delta\boldsymbol{\alpha}_0 = [0, -40, 0, 4, 0, 4]^{\mathrm{T}}$ $a\delta\boldsymbol{\alpha}_f = [0, -5, 0, 0.5, 0, 0.5]^{\mathrm{T}}$	48
Far-range 2	J_e	AO	$a\delta\boldsymbol{\alpha}_0 = [0, -5, 0, 0.5, 0, 0.5]^{\mathrm{T}}$ $a\delta\boldsymbol{\alpha}_f = [0, -1, 0, 0.25, 0, 0.25]^{\mathrm{T}}$	24
Mid-range	J_e	A+R	$a\delta\boldsymbol{\alpha}_0 = [0, -1, 0, 0.25, 0, 0.25]^{\mathrm{T}}$ $a\delta\boldsymbol{\alpha}_f = [0, -0.5, 0, 0.15, 0, 0.15]^{\mathrm{T}}$	20

4.3. GNC architecture and simulation results

The GNC functions described in the previous subsections represent the core of the autonomous R-GNC from far to mid range. However, considering that the servicer at the start of the rendezvous relies on a poor estimate of the relative state based on TLE, the guidance and control solution applied in an open loop fashion will not be a feasible options. Therefore, the strategy implemented relies on a shrinking horizon Model Predictive Control (MPC) architecture, where the guidance and control solution is computed after each reconfiguration guidance node t_i keeping the final time t_f fixed. The present solution has been successfully implemented in the AVANTI demonstration, more details in [26]. The GC solution is then progressively updated based on the improvement and convergence of the navigation solution. This scheme will allow the reduction of errors with respect to an open-loop implementation of the GC scheme, at a very low on-board computational expense thanks to the chosen approach to solve the guidance solution. The preliminary simulation campaign to validate the approach R-GNC system is performed considering the phases of the rendezvous shown in Table 4. Here, the servicer is considered at a separation of approximately 40 km behind the target and a total reconfiguration time of 92 periods is allocated for reducing the separation up to few hundreds of meters. In this preliminary simulation campaign, three phases are defined enforcing the final ROE state as a passively safe orbits. Particularly, the observability enhancement strategy within the guidance solution is used in the first phase where the uncertainties in the target position knowledge are more pronounced.

The performance of the GNC system are obtained from a Monte Carlo (MC) simulation campaign in an high-fidelity environment. The simulations are performed considering the servicer and target orbital dynamics considering a 180 × 180 gravity model and osculating to mean conversions of relative orbital elements to map the GNC solutions designed in the mean ROE space to the osculating conditions in orbit [52]. The dynamics are integrated using an eighth-order Dormand-Prince scheme with fixed step of 10 s. The drag effects are neglected at first iteration due to the high altitude orbits considered. The guidance time discretisation is performed considering guidance nodes spaced by 4 revolutions in the far-range 1 phase. The nodes with non-zero observability weight are the first three of the mesh. One hundred MC simulations with different observability enhancement constant $k_{obs,j}$ of Eq. (24) were performed. To assess the GNC performance two

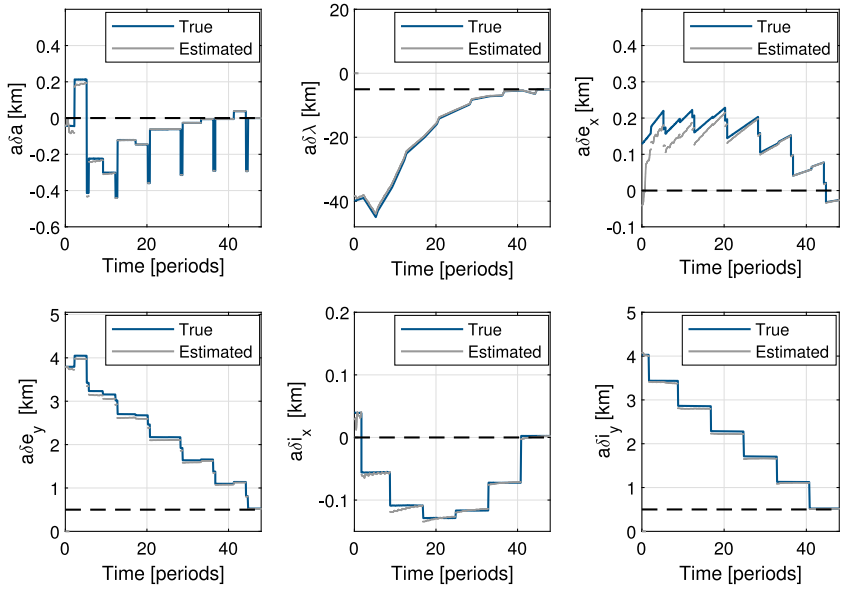

Fig. 2. Real mean ROE (blue) and estimated ROE (grey) time histories during a one example of far-range rendezvous using the R-GNC routines considering $k_{obs} = 0.04$.

Table 5
Results of simulations in terms of errors for different cases of k_{obs}. The reported values represent the mean values over the 100 MC runs of the GNC.

$\mathbf{k_{obs}}$ [-]	$\bar{e}_{\delta\hat{\lambda}_f}$ [m]	$\bar{e}_{\delta\lambda_f}$ [m]	δv_{tot} [m/s]
0	209.6	1042.6	5.22
0.01	177.0	817.9	5.23
0.02	198.3	661.8	5.24
0.03	121.7	504.2	5.27
0.04	102.2	389.6	5.32
0.05	99.1	307.7	5.34

different metrics were introduced and are reported as follows.

$$\bar{e}_{\delta\hat{\lambda}_f} = \frac{\sum_j^{N_{MC}} |\delta\hat{\lambda}(t_f) - \delta\lambda_{real}(t_f)|}{N_{MC}}, \quad \bar{e}_{\delta\lambda_f} = \frac{\sum_j^{N_{MC}} |\delta\lambda_f - \delta\lambda_{real}(t_f)|}{N_{MC}} \tag{28}$$

The navigation errors $\bar{e}_{\delta\hat{\lambda}_f}$ are defined considering the average between the N_{MC} MC runs of the absolute values of the difference between the estimated relative longitude from the filter and the its real value. While the control errors $\bar{e}_{\delta\lambda_f}$ are defined as the average between the final real value of relative longitude and the target value $\delta\lambda_f$. Table 5 shows the statistics of the simulations for the different cases were the observability constants $k_{obs,q}$ are considered with the same for all the nodes within one approach. It can be appreciated how increasing the observability constants k_{obs} values, the navigation and control errors decrease at the expense of a more demanding GC solution in terms of delta-v cost. The delta-v cost is evaluated as the sum of the cost of each tangential and normal separate manoeuvres. For this study, the observability constants are chosen with value of 0.04 as a trade-off considering the reduction of navigation error up to 50% of the case with $k_{obs} = 0$, provided a limited increase of delta-v cost. In Fig. 2, the ROE time histories during the far-range 1 phase for one GNC solution with $k_{obs} = 0.04$ is shown, together with the filter estimates. Fig. 3 and Fig. 4 show respectively the trajectory in the orbital elements space and the manoeuvre placement in time for the same GNC solution. In Fig. 5 the time history of the filter estimate $a\delta\hat{\alpha}$ error with respect to the true relative state is shown for the same simulation case of Fig. 2, also displaying the error envelope obtained from the covariance matrix diagonal output of the EKF in light red.

Table 6
Far-range 2 and mid-range approach results. The results reported refer to the mean values out of the 100 MC simulations performed.

	Nav. errors	Control errors	Cost
Phase	$\bar{e}_{\delta\hat{\lambda}_f}$ [m]	$\bar{e}_{\delta\lambda_f}$ [m]	δv_{tot} [m/s]
Far-range 2	17.84	14.38	0.435
Mid-range	0.13	0.57	0.148

The effect on the trajectory of the observability enhancement included directly in the analytic guidance computed in the ROE space influences the trajectory in RTN by maintaining for longer time in the progressive approach a larger separation in the RN plane, as shown in Figs. 6 and 7. This behaviour is related to the fact that the guidance tries to maximise the change of the line-of-sight vectors between the first three guidance nodes. The subsequent phases of the R-GNC approach of Table 4 are simulated considering the functioning of the LiDAR system providing range measurements in the mid-range phase. The simulations results statistics for 100 Monte-Carlo (MC) simulations are shown in Table 6. Fig. 8 demonstrates the improvement of the navigation solution in the mid-range phase, thanks to the LiDAR range measurements taken four times per revolution.

4.4. Safety considerations

The safety of the relative approach to the uncooperative target is of utmost importance for the successful completion of the rendezvous operations. In this work the relative approach is designed to maintain a passively safe trajectory along the whole approach [25]. Firstly, the passive safe feature is enforced providing given initial and final conditions of the intermediate phases in Table 4 of the approach characterised by E/I vector separation in the parallel configuration. In this way, the trajectory over the whole approach is forced to meet the E/I perfect separation at the intermediate phases boundaries before reducing further the separation towards the target in the next phase. Moreover, along the trajectory computed by the guidance routine, the minimum RN separation at the guidance nodes is evaluated. The definition introduced by Gaias et al. [53] is used which takes into account the translation in the radial direction due to a non-vanishing relative semi-major axis. In the cases where the intermediate guidance nodes drive the minimum RN distance below the defined threshold,

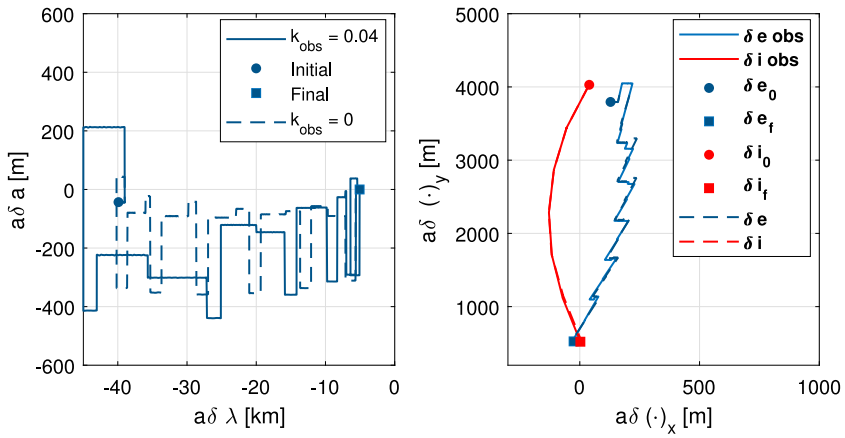

Fig. 3. Trajectory in the $\delta a - \delta\lambda$ space (left) and $\delta(\cdot)_x - \delta(\cdot)_y$ space (right) of the ROE evolution for one example of far-range rendezvous using the R-GNC routines considering $k_{obs} = 0.04$.

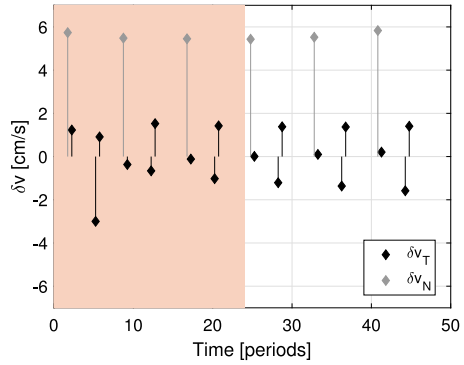

Fig. 4. Impulsive delta-v distribution over time for one example of far-range rendezvous using the R-GNC routines considering $k_{obs} = 0.04$. Orange shaded area represents the guidance nodes time window where the observability enhancement is applied. (For interpretation of the references to colour in this figure legend, the reader is referred to the web version of this article.)

the guidance will act on limiting the magnitude of the ROE jumps required by the guidance scheme, by considering enough configuration nodes at guidance level to limit and an appropriately long configuration final time t_f. The increase of the time available for the configuration has the effect of reducing the relative semi-major axis magnitude to reduce the separation in relative longitude, hence reducing the radial drift of the RN ellipse. The threshold for this phase is considered as a circular Keep-Out-Zone (KOZ) in the RN plane, with radius four times the target's largest dimension. In particular, a KOZ radius of 16 meters and 36 meters are considered respectively for the LT and HT test cases in Table 1. Fig. 9 shows the minimum distance in the RN plane during one mid range trajectory.

5. Inspection

After the reduction of the servicer-target separation up to few hundred meters with the R-GNC, the servicer has acquired a reliable estimate and knowledge of the translational relative state of the target. However, to proceed with the close-proximity operations, a dedicated inspection phase is required to complement the knowledge of the target with in-orbit observations of the target's pose and physical characteristics. An accurate knowledge of these conditions is mandatory to proceed with the closer operation. In this section, the trajectory design of this phase is presented with focus on autonomous safety operations and efficiency in the observation capabilities from the trajectory planning point of view.

5.1. Walking safety ellipse strategy

The paradigm used to design the relative trajectories for inspection is to exploit the natural relative dynamics to obtain the required fly-around of the target body. The strategy adopted consists in the use of Walking Safety Ellipses (WSE) to fly around the envelope around the target in the RTN frame. These particular trajectories can be defined in the ROE space, considering a E/I separation and a residual semi-major axis difference $a\delta a$. This design will result in a drifting spiralling trajectory around the local velocity axis, with a guaranteed minimum safe separation in the RN plane. A sequence of these trajectories will be used to efficiently observe the target from different point of views. The design is performed by selecting multiple drifting WSE with the features: (1) different drift direction with respect to the target, (2) different fundamental sizes of safety ellipses, (3) different eccentricity of the relative orbit (phasing of the relative eccentricity and inclination vector). The direction of drift are denoted as + and - representing respectively the target drifting from negative to positive and positive to negative relative longitude with respect to the target. The relative semi-major axis of each of the orbits is obtained considering the drift from a value of $\delta\lambda$ to the symmetric condition at the other side of the target in a fixed time of eight orbital periods. The relative eccentricity and inclination vectors are expressed as:

$$\delta\mathbf{e} = \begin{bmatrix}\delta e_x \\ \delta e_y\end{bmatrix} = \begin{bmatrix}\delta e \cos\phi \\ \delta e \sin\phi\end{bmatrix} \quad \delta\mathbf{i} = \begin{bmatrix}\delta i_x \\ \delta i_y\end{bmatrix} = \begin{bmatrix}\delta i \cos\theta \\ \delta i \sin\theta\end{bmatrix} \tag{29}$$

The phasing angles ϕ and θ define the E/I separation condition. Particularly, ensuring the parallelism (or anti-parallelism of the vectors) the passive safety as minimum separation in the RN plane can be achieved [25]. The magnitudes of these vectors, δe and δi, will then be used to control this minimum separation along the drift WSE to guarantee observation of the target at different distances.

Together with the proper sizing of the WSEs, the relative eccentricity and inclination vector phase angles are selected to guarantee proper illumination conditions. The particular value ϕ, argument of perigee of the relative orbit, defines the relative position of the servicer with respect to the target at a particular mean argument of latitude (u) along the absolute orbit, which defines the illumination conditions. Accordingly, ϕ is the key parameter to assess illumination conditions. To that end, the servicer is assumed in a target-pointing mode (i.e, with boresight of the relative navigation sensors' suite directed towards the target). Then the angle α_S between the Sun direction in the RTN frame and the servicer position vector in the RTN frame is considered. When the Sun direction is opposite to the servicer position vector ($\alpha \approx 180$ deg), the target is considered to be in a poor illumination condition due to either the Sun blinding the visible camera FOV or

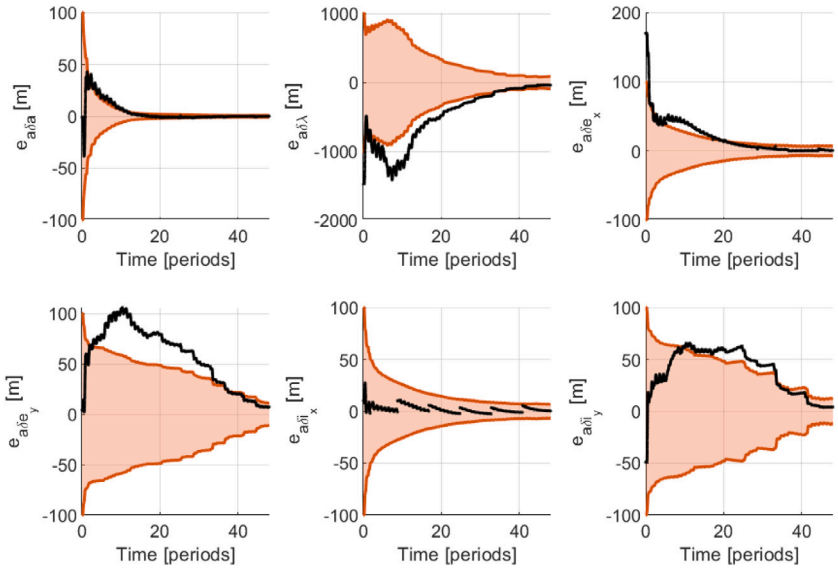

Fig. 5. Relative navigation ROE errors time histories during the far-range rendezvous using the R-GNC routines considering $k_{obs} = 0.04$.

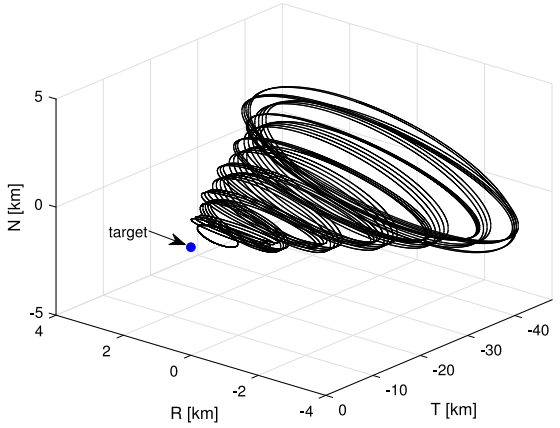

Fig. 6. Far-range trajectory in RTN frame considering no observability enhancement.

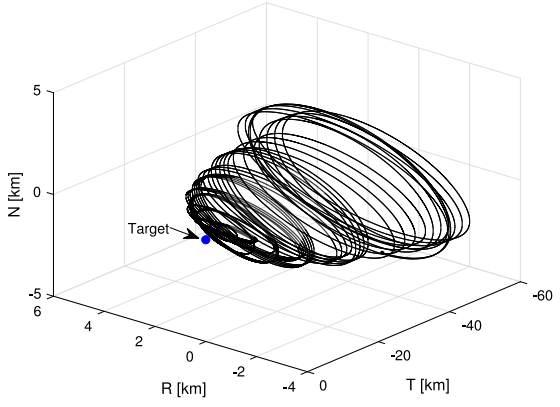

Fig. 7. Far-range trajectory in RTN frame considering $k_{obs} = 0.04$.

the surfaces of the target facing the servicer not being sufficiently illuminated. A cone of poor visibility (referred here as *blind regions*) around the condition of $\alpha = 180$ deg is considered with aperture of ± 60 deg to account for relative illumination of target surface and camera FOV. Blind zones are also extended to values of mean argument of latitudes where the formation is in the Earth's eclipse condition. Therefore, by changing the relative phasing of the relative eccentricity and inclination vectors, the blind regions occupy different portions of the relative orbit, therefore guaranteeing to observe the target under different illumination conditions.

Table 7
WSEs parameters selected for the inspection sequence for LT (OneWeb Arrow platform).

	$\|\|a\delta\mathbf{e}\|\| = \|\|a\delta\mathbf{i}\|\|$ [m]	$\phi = \theta$ [deg]	$a\delta a$ [m]	$a\delta\lambda$ [m]
WSE1+	150	0	−10.61	−500
WSE1-	150	90	10.61	500
WSE2+	75	90	−5.30	−250
WSE2-	75	180	5.30	250
WSE3+	50	180	−5.30	250
WSE3-	50	270	5.30	250

The sequence preliminary designed for the inspection of the light target platform is reported in Table 7, where the E/I separation with parallel relative eccentricity and inclination vector is enforced.

In the design of Table 7, the keep-out-zone considered to define WSE size is considered as in Section 4 as a circular region in the RN plane with radius of four times the longest dimension of the target. In this phase, the position uncertainties from the navigation solution are expected to be smaller than in the far-mid approach phase. Nonetheless, the conservative choice of maintaining a constant KOZ size regardless of the position uncertainties was made, to account for possible contingencies and non-nominal behaviour during operations. In Table 7 is shown how the phase angle ϕ for each nominal WSE is changed of 90 degrees from the previous WSE, to exploit different illumination conditions. The trajectories shown in Fig. 10 show the effect of the change in the ϕ angle between subsequent WSEs, displaying in magenta the blind regions of the WSE2+ (top) and WSE2- (bottom). Clearly the design of the phasing angles of WSE must account for the relative geometry of orbital plane and Sun direction at the inspection operations. However, assuming that the Sun direction in the inertial Earth centred frame does not significantly change during an inspection sequence the optimisation of the WSE conditions can be designed offline prior the approach and can be tailored for each rendezvous within the ADR service.

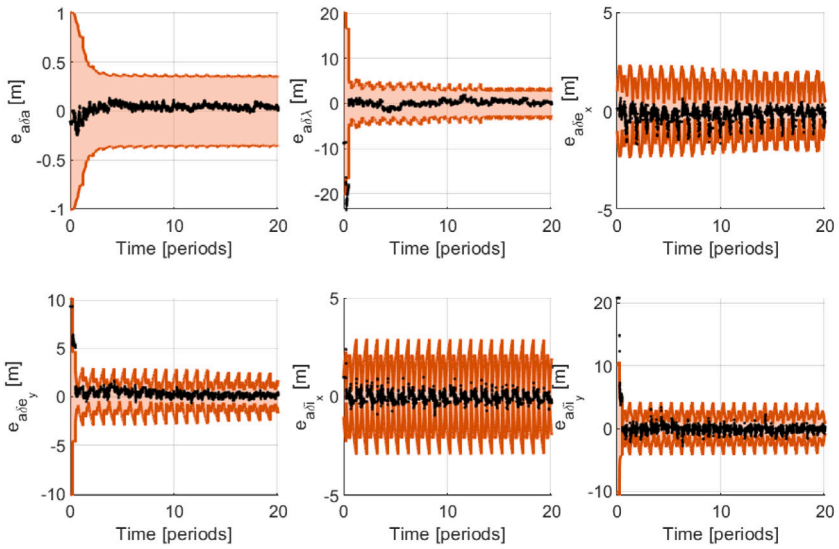

Fig. 8. Relative navigation ROE errors time histories during the mid-range rendezvous using the R-GNC routines complemented by the range measurement from LiDAR sensor.

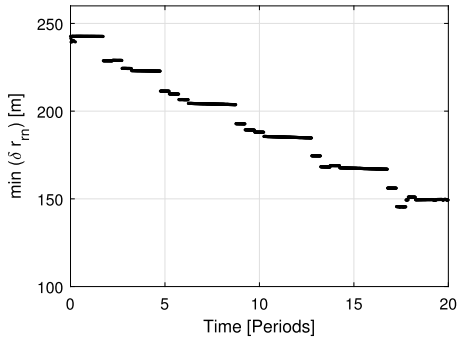

Fig. 9. Minimum RN separation of the relative trajectory along the mid-range phase.

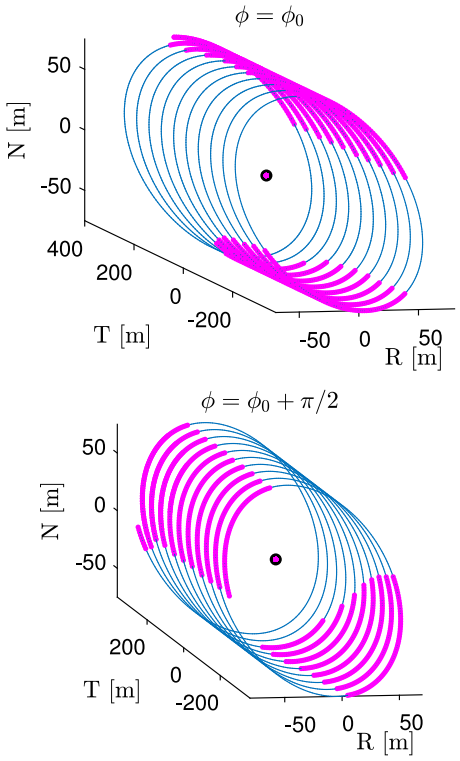

Fig. 10. WSE2+ and WSE2- trajectory in RTN. Magenta regions represent the blind spots for visible camera acquisition due to eclipses and poor target illumination.

5.2. Safe impulsive transfers design

The transfer between the foreseen WSE trajectories is performed autonomously on-board exploiting the analytic optimal delta-v schemes described in [45]. In addition to fuel-optimal considerations, in this work passive safety conditions are enforced during the whole transfer, instead of only at the boundary conditions of WSEs. This aspect, in fact, is crucial to enable safe autonomous operations. To guarantee the required E/I separation, the out-of-plane manoeuvres are performed at the same mean argument of latitudes of in-plane ones. Accordingly, the minimum distance of the spiral to the target in the RN plane can be expressed as:

$$r_{RN,min} = min\{\delta e - |\delta a|, \delta i\} \tag{30}$$

In the implementation of the inspection sequence, two different types of transfer are required: (1) change of phase angle ϕ and δa without changing the size of the WSE, (2) change of size of the WSE (i.e., δe and δi) and δa without changing the phase angle. Fig. 11 (left) shows the trajectories in the former case during the impulsive manoeuvre sequence to move from WSE1+ to WSE1-, where only a change in the ROE vector phasing $\phi = \theta$ is sought. As it is required by the scheme, Fig. 11 how the relative eccentricity and inclination vectors remain parallel by design along the three manoeuvre sequence. Here three out-of-plane manoeuvres are designed in correspondence of the three in-plane manoeuvres, the latter obtained with the fuel-optimal design described in [45]. Fig. 12 shows instead the impulsive reconfiguration transfer between WSE1- to WSE2+, where instead the magnitude of eccentricity and inclination vector is performed to reduce the distance to the target in the RN plane. As a result, the delta-v spent for each reconfiguration within the inspection sequence is reported in Table 8.

6. Rigid capture preparation operations

The last phase described in this work begins after that the inspection sequence has provided accurate information on the dynamic and physical state of the target, see Fig. 1. The operations design of this section deal with the situations where the target presents a fast tumbling motion, generating risks for the safe and successful close approach and

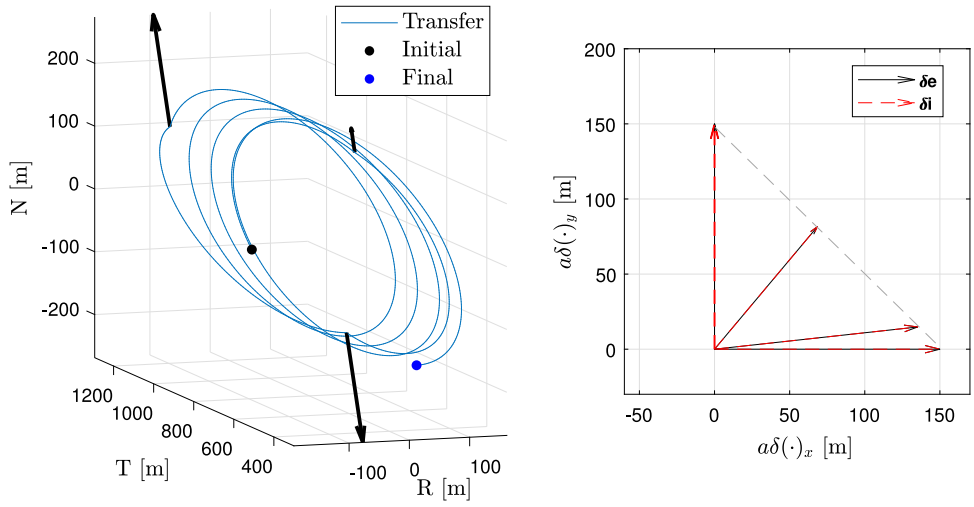

Fig. 11. Transfer reconfiguration trajectory between WSE1- and WSE1+ (left). Arrows represent the impulsive manoeuvres directions and magnitude in the RTN frame, magnitude not in scale. Evolution of the relative eccentricity and inclination vectors in the ROE space during the three phase change manoeuvre sequence (right).

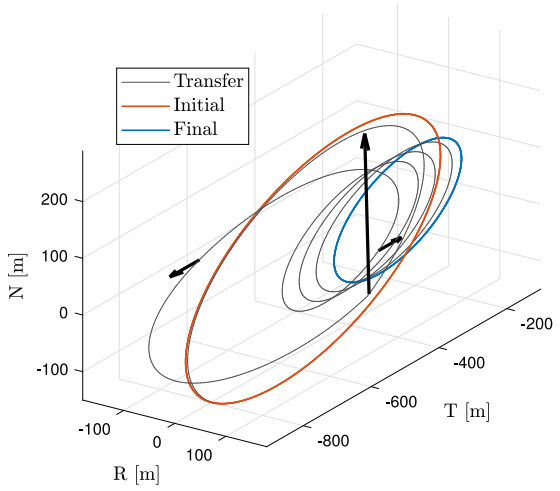

Fig. 12. Transfer reconfiguration trajectories between WSE1+ and WSE2-.Arrows represent the impulsive manoeuvres directions and magnitude in the RTN frame, magnitude not in scale.

Table 8
Expenditure of delta-v for the reconfiguration manoeuvres required for the inspection sequence of Table 7.

Transfer	δv_{tot} [m/s]
WSE1+ ⇒WSE1−	0.227
WSE1− ⇒WSE2+	0.110
WSE2+ ⇒WSE2−	0.113
WSE2− ⇒WSE3+	0.037
WSE3+ ⇒WSE3−	0.076
Total	0.563

capture. The inclusion of this phase is considered instrumental for the design of the ADR service under study, since it provides the potential to increase the safe capture chances of a target debris regardless its conditions. In this way, the ADR service will be capable of approaching and removing/servicing more failed targets within the constellation without having to oversize the servicer's systems to the most challenging scenario, i.e. synchronisation for the fastest angular rates, or aborting the missions after the inspection phase.

The rigid capture preparations operations foresees a detumbling strategy to reduce the angular rate of the free motion of the debris. Here the strategy adopted foresees the use of the plume impingement effects of the servicer's thrusters to provide torques to the target platform. The choice is motivated by the capability of providing the required control torques from a safe distance from the target, and the negligible impact on the system design of the servicer since it will employ the already available on-board thrusters. In such operations, the servicer's thruster plume are used to create surface forces, hence torques, on the target tumbling body. The control algorithm is focused then on deciding the firing times and thrust directions of the plume such that the torques on the target are capable of reducing its angular rate. During the impingement control operations, the servicer is assumed to be in a station-keeping position R_{safe} at +T just outside the keep-out zone, defined as a spherical region around the target. In this way, the thruster plume action designed to produce torques on the target will also contribute to reducing orbital energy of the target with forces in the -T direction, aiding the future de-orbiting operations. The control the servicer's thruster pointing control to generate detumbling torques on the target is based on the algorithm explored in [39]. In this algorithm, only one thruster of the servicer is used to generate control contactless torque. The main features of the algorithm are the on-board representation of the plume impingement torque with an analytic pressure model of the thruster plume and the selection of the candidate pointing towards the target body. The analytic plume model describes the pressure inside the plume as [54]:

$$P\left(\theta_t, r\right) = C\, e^{\frac{-\theta_t}{2\theta_{t,0}}} r^{-2} \tag{31}$$

Where θ_t is angle measured from the thruster centre line, r is the distance from the thruster nozzle exit. The half cone angle $\theta_{t,0}$ represents the 1σ width of the plume, while the constant C is derived from the thrust force F from continuity considerations. The force generated on a surface impinged by the plume is modelled considering a diffuse reflection of hyper-thermal flow. The analytic model used is the one employed in [37]:

$$d\mathbf{F} = -P\,(r,\theta)\cos\gamma dS\,\left[\left(1-c_s\right)\,\mathbf{S} + \mathbf{2}(c_s\cos\gamma + \frac{1}{3}c_d)\mathbf{N}\right] \tag{32}$$

where γ represents the angle between the surface normal and the thruster centre line and dS the area of the surface element. The vector $\hat{S}$ and $\hat{N}$ are respectively the line of sight vector of the thruster centre line and the surface normal vector. The coefficients c_d and c_s represent the diffuse and specular coefficient respectively [37]. The plume model parameters and thruster characteristics are reported in

Table 9
Impingement model parameters and operational distance.

Parameter	Value
F	10 N
θ_0	12 deg
c_s	0.03
c_d	0.97
R_{safe} (LT)	16 m
R_{safe} (HT)	36 m

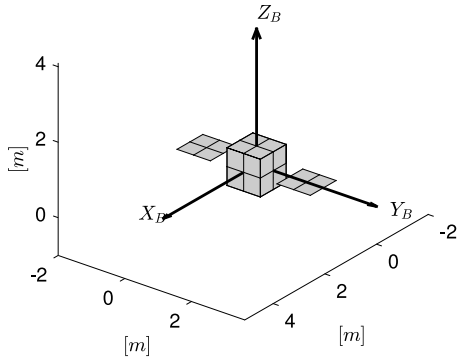

Fig. 13. Simplified model of Light Target (LT) platform, representative of OneWeb constellation.

Table 9. The control algorithm computes the thruster pointing towards the target considering the capability at each instant to generate a predefined guidance torque for detumbling. The guidance torque is obtained considering the target rotational angular momentum vector expressed in the RTN frame as follows [36,39]:

$$T_g = -K_d \mathbf{h}_L \tag{33}$$

where K_d is a constant gain matrix.

The detumbling control has been simulated for the baseline constellations light and heavy targets. Figs. 13 and 14 show the simplified models of the constellations satellites, generated with additions of elementary surfaces and representing only the spacecraft body and solar panels. Different operational distances for the two constellation baseline test cases are considered according to the respective keep-out zones. Fig. 15 shows the effect of plume impingement control in the detumbling of the LT case considering different initial tumbling rates magnitude. It can be noted how the strategy is effective in reducing the initial angular rate from up to 11 deg/s. The higher initial tumbling rate requires longer stabilisation time needed and the greater propellant expenditure of the impingement operations.

A simulation campaign was conducted to evaluate the effectiveness of the selected strategy, considering three different initial angular rate states. For each of the tumbling conditions, one hundred different simulations were performed for different initial attitude configuration. The simulation campaign results are reported in Table 10, where the average and maximum propellant expenditure used by the impingement thruster is reported, denoted respectively with $\overline{m}_p$ and $m_{p,max}$. The different tumbling motions are represented by the initial body angular rate vector $\boldsymbol{\omega}_{BN,0}$. The value of ϵ represent a small residual angular rate in the remaining direction for each motion. The value is taken in the simulations as 0.5 deg/s. It can be noted how the tumbling motions with initial body angular rate parallel to the y directions requires approximately double the propellant to be controlled. An expected result considering the symmetry axis and geometry of the targets, which limit the available surfaces to generate torque along that axis.

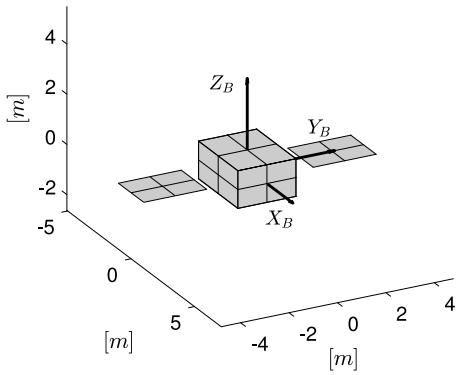

Fig. 14. Simplified model of Heavy Target (LT) platform, representative of GLOBALSTAR constellation.

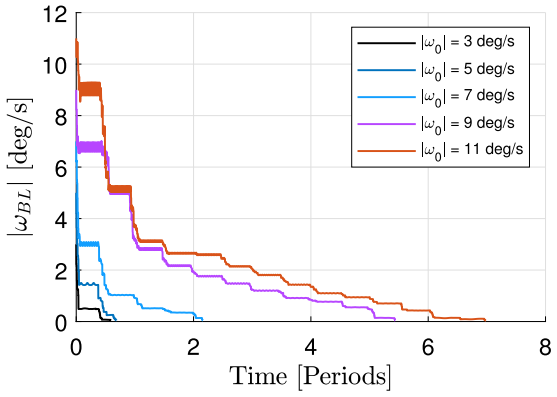

Fig. 15. Time history of the magnitude of angular rates of the light target under the influence of the plume impingement control considering different initial conditions.

Table 10
Propellant expenditure of the detumbling operations for the two different constellation baseline satellites.

	$\omega_{BN,0}$ [deg/s]	$[\epsilon,\epsilon,5]^T$	$[\epsilon,5,\epsilon]^T$	$[5,\epsilon,\epsilon]^T$
LT	$\overline{m}_p$[kg]	0.82	2.58	1.00
	$m_{p,max}$ [kg]	1.35	2.99	1.54
HT	$\overline{m}_p$[kg]	1.24	3.19	1.12
	$m_{p,max}$ [kg]	1.85	3.52	1.48

7. Conclusions

In this work, the phase 0/A design of the rendezvous and proximity operations for an active debris removal service for large constellations was presented. The challenges tackled all along the phases analysed comprehend the improvement the robustness of the design with respect to targets' conditions, overall mission safety, and autonomy. In the far-range phase, a novel analytic guidance solution was developed to improve the accuracy of the onboard angles-only navigation solution, demonstrating the feasibility of cutting navigation and control errors up to 50% with a little increase on the delta-v spent. A scheme for the inspection was then presented capable of improving the illumination conditions for target observations, and guaranteeing passive safety along the whole sequence. At last, the inclusion of a preparation for rigid capture phase with contactless detumbling demonstrated the capability of the servicer to damp target's residual angular motions up to 11 deg/s enabling the safe capture operations for a wider candidates among the failed constellation satellites without impacting the design of the servicer prior launch. In the future the detailed design of the

close-approach and capture phases are envisioned, together with the further validation of the GNC strategies presented here in suitable testing environments.

Declaration of competing interest

The authors declare that they have no known competing financial interests or personal relationships that could have appeared to influence the work reported in this paper.

Acknowledgements

The research leading to these results has received funding from the European Research Council (ERC) under the European Union's Horizon2020 research and innovation programme as part of project COMPASS (Grant agreement No 679086), https://www.compass.polimi.it/, and the ESA Sunrise, Provision of Engineering Services to OneWeb in support of ESA ARTES Public Private Partnership "SUNRISE" between ESA and OneWeb, OW-SUN-SOW-00003. The contribution of Dr. Gabriella Gaias is funded by the European Union's Horizon 2020 research and innovation programme under the Marie-Sklodowoska Curie grant ReMoVE (grant agreement nr 793361).

References

[1] ESA Space Debris Office, ESA's Annual Space Environment Report, Tech. rep., ESA, 2021.

[2] D.J. Kessler, Collisional cascading: The limits of population growth in low earth orbit, Adv. Space Res. 11 (12) (1991) 63–66, http://dx.doi.org/10.1016/0273-1177(91)90543-S, URL https://www.sciencedirect.com/science/article/pii/027311779190543S.

[3] B. Bastida Virgili, J. Dolado, H. Lewis, J. Radtke, H. Krag, B. Revelin, C. Cazaux, C. Colombo, R. Crowther, M. Metz, Risk to space sustainability from large constellations of satellites, Acta Astronaut. 126 (2016) 154–162, http://dx.doi.org/10.1016/j.actaastro.2016.03.034, URL https://www.sciencedirect.com/science/article/pii/S0094576516300820.

[4] J. Radtke, C. Kebschull, E. Stoll, Interactions of the space debris environment with mega constellations—Using the example of the OneWeb constellation, Acta Astronaut. 131 (2017) 55–68, http://dx.doi.org/10.1016/j.actaastro.2016.11.021, URL https://www.sciencedirect.com/science/article/pii/S009457651630515X.

[5] J.-C. Liou, N. Johnson, N. Hill, Controlling the growth of future LEO debris populations with active debris removal, Acta Astronaut. 66 (5) (2010) 648–653, http://dx.doi.org/10.1016/j.actaastro.2009.08.005, URL http://www.sciencedirect.com/science/article/pii/S0094576509003981.

[6] S. Le May, S. Gehly, B. Carter, S. Flegel, Space debris collision probability analysis for proposed global broadband constellations, Acta Astronaut. 151 (2018) 445–455, http://dx.doi.org/10.1016/j.actaastro.2018.06.036, URL https://www.sciencedirect.com/science/article/pii/S0094576518304375.

[7] A. Rossi, A. Petit, D. McKnight, Short-term space safety analysis of LEO constellations and clusters, Acta Astronaut. 175 (2020) 476–483, http://dx.doi.org/10.1016/j.actaastro.2020.06.016, URL https://www.sciencedirect.com/science/article/pii/S0094576520303830.

[8] B. Revelin, J.-C. Dolado-Perez, Risk induced by the uncatalogued space debris population in the presence of large constellations, J. Br. Interplanet. Soc. 70 (2017) 2–4.

[9] H.G. Lewis, Evaluation of debris mitigation options for a large constellation, J. Space Saf. Eng. 7 (3) (2020) 192–197.

[10] J.-C. Liou, M. Matney, A. Vavrin, A. Manis, D. Gates, NASA ODPO's large constellation study, Orbital Debris Q. News 22 (3) (2018) 4–7, cited by: 15. URL https://www.scopus.com/inward/record.uri?eid=2-s2.0-85078269434&partnerID=40&md5=98c028177b419fe91847ce71ad3f4ba6.

[11] C. Colombo, S. Huang, G. Borelli, F. Cavenago, M. Nugnes, J. Gonzalo Gòmez, G. Gaias, M. Massari, L. Vallini, M. Petit, et al., Mission analysis and design for an active debris removal service for large constellations, in: Proc. of 8th European Conference on Space Debris, ESA/ESOC, 2021.

[12] S. Huang, C. Colombo, J.L. Gonzalo, A. Masserini, M. Nugnes, L. Vallini, M. Petit, Preliminary mission analysis of active debris removal service for large constellations, in: 71st International Astronautical Congress, 2020.

[13] J. Forshaw, R.d.V. van Steenwijk, S. Wokes, S. Ainley, A. Bradford, J. Auburn, C. Blackerby, N. Okada, Preliminary design of an end-of-life ADR mission for large constellations, in: Proc. International Astronautical Congress IAC, 2019.

[14] H. Brettle, J. Forshaw, J. Auburn, C. Blackerby, N. Okada, Towards a future debris removal service: evolution of an ADR business model, in: 70th International Astronautical Congress, 2019.

[15] H. Brettle, H. Lewis, T. Harris, M. Lindsay, Assessing debris removal services for large constellations, in: Proc. of 8th European Conference on Space Debris, ESA/ESOC, 2021.

[16] J. Šilha, J.-N. Pittet, M. Hamara, T. Schildknecht, Apparent rotation properties of space debris extracted from photometric measurements, Adv. Space Res. 61 (3) (2018) 844–861, http://dx.doi.org/10.1016/j.asr.2017.10.048, URL https://www.sciencedirect.com/science/article/pii/S027311771730786X.

[17] D. Kucharski, G. Kirchner, F. Koidl, C. Fan, R. Carman, C. Moore, A. Dmytrotsa, M. Ploner, G. Bianco, M. Medvedskij, A. Makeyev, G. Appleby, M. Suzuki, J.-M. Torre, Z. Zhongping, L. Grunwaldt, Q. Feng, Attitude and spin period of space debris envisat measured by satellite laser ranging, IEEE Trans. Geosci. Remote Sens. 52 (12) (2014) 7651–7657, http://dx.doi.org/10.1109/TGRS.2014.2316138.

[18] L.B.M. Sagnières, I. Sharf, Long-term rotational motion analysis and comparison to observations of the inoperative envisat, J. Guid. Control Dyn. 42 (2) (2019) 364–376, http://dx.doi.org/10.2514/1.G003647, arXiv:https://doi.org/10.2514/1.G003647.

[19] R. Biesbroek, L. Innocenti, A. Wolahan, S.M. Serrano, e. Deorbit–ESA's active debris removal mission, in: Proceedings of the 7th European Conference on Space Debris, ESA Space Debris Office, 2017, p. 10.

[20] R. Biesbroek, S. Aziz, A. Wolahan, S.-f. Cipolla, M. Richard-Noca, L. Piguet, The clearspace-1 mission: Esa and clearspace team up to remove debris, in: Proc. 8th European Conference on Space Debris, 2021, pp. 1–3.

[21] T. Yamamoto, J. Matsumoto, H. Okamoto, R. Yoshida, C. Hoshino, K. Yamanaka, Pave the way for active debris removal realization: JAXA commercial removal of debris demonstration (CDR2), in: Proc. 8th European Conference on Space Debris, 2021.

[22] M. Ganet, I. Quinquis, J. Bourdon, P. Delpy, ATV GNC during rendezvous with ISS, 2002.

[23] T. Mulder, Orbital express autonomous rendezvous and capture flight operations, part 2 of 2: Ar&c exercise 4,5, and end-of-life, in: AIAA/AAS Astrodynamics Specialist Conference and Exhibit, http://dx.doi.org/10.2514/6.2008-6768, arXiv:https://arc.aiaa.org/doi/pdf/10.2514/6.2008-6768. URL https://arc.aiaa.org/doi/abs/10.2514/6.2008-6768.

[24] I. Kawano, M. Mokuno, T. Kasai, T. Suzuki, Result of autonomous rendezvous docking experiment of engineering test satellite-VII, J. Spacecr. Rockets 38 (1) (2001) 105–111, http://dx.doi.org/10.2514/2.3661, arXiv:https://doi.org/10.2514/2.3661.

[25] S. D'Amico, O. Montenbruck, Proximity operations of formation-flying spacecraft using an eccentricity/inclination vector separation, J. Guid. Control Dyn. 29 (3) (2006) 554–563, http://dx.doi.org/10.2514/1.15114, arXiv:https://doi.org/10.2514/1.15114.

[26] G. Gaias, J.-S. Ardaens, Flight demonstration of autonomous noncooperative rendezvous in low earth orbit, J. Guid. Control Dyn. 41 (6) (2018) 1337–1354.

[27] M. Vavrina, C.E. Skelton, K. Deweese, B. Naasz, D. Gaylor, C. D'souza, Safe rendezvous trajectory design for the restore-l mission, in: Advances in the Astronautical Sciences, 2019, pp. 3649–3668.

[28] D.C. Woffinden, D.K. Geller, Observability criteria for angles-only navigation, IEEE Trans. Aerosp. Electron. Syst. 45 (3) (2009) 1194–1208, http://dx.doi.org/10.1109/TAES.2009.5259193.

[29] J. Grzymisch, W. Fichter, Optimal rendezvous guidance with enhanced bearings-only observability, J. Guid. Control Dyn. 38 (6) (2015) 1131–1140, http://dx.doi.org/10.2514/1.G000822, arXiv:https://doi.org/10.2514/1.G000822.

[30] E.C. Team, e.Inspector CDF Study Report - Assessment of an ENVISAT Imaging Mission as a Precursor to a Potential ENVISAT Deorbit, Tech. rep., European Space Agency (ESA), 2017.

[31] S. Silvestrini, J. Prinetto, G. Zanotti, M. Lavagna, Design of robust passively safe relative trajectories for uncooperative debris imaging in preparation to removal, vol. 175, 2021, pp. 4205–4222, URL https://www.scopus.com/inward/record.uri?eid=2-s2.0-85126240899&partnerID=40&md5=6a51911e8e10ed060ac72ea48b7bbcb5,

[32] R. Kumar, R.J. Sedwick, Despinning orbital debris before docking using laser ablation, J. Spacecr. Rockets 52 (4) (2015) 1129–1134, http://dx.doi.org/10.2514/1.A33183, arXiv:https://doi.org/10.2514/1.A33183.

[33] T. Bennett, D. Stevenson, E. Hogan, H. Schaub, Prospects and challenges of touchless electrostatic detumbling of small bodies, Adv. Space Res. 56 (3) (2015) 557–568, http://dx.doi.org/10.1016/j.asr.2015.03.037, advances in Asteroid and Space Debris Science and Technology - Part 1. URL http://www.sciencedirect.com/science/article/pii/S0273117715002392.

[34] M. Vetrisano, N. Thiry, M. Vasile, Detumbling large space debris via laser ablation, in: IEEE Aerospace Conference Proceedings 2015, 2015, http://dx.doi.org/10.1109/AERO.2015.7119051.

[35] N. Ortiz, S. Walker, M. Jankovic, J.M. Romero Martin, F. Kirchner, M. Vasile, Control analysis for a contactless de-tumbling method based on eddy currents: problem definition and approximate proposed solutions, 2016, http://dx.doi.org/10.2514/6.2016-0642.

[36] Y. Nakajima, H. Tani, T. Yamamoto, N. Murakami, S. Mitani, K. Yamanaka, Contactless space debris detumbling: A database approach based on computational fluid dynamics, J. Guid. Control Dyn. 41 (9) (2018) 1906–1918, http://dx.doi.org/10.2514/1.G003451, arXiv:https://doi.org/10.2514/1.G003451.

[37] T.V. Peters, D. Escorial Olmos, COBRA contactless detumbling, CEAS Space J. 8 (3) (2016) 143–165, http://dx.doi.org/10.1007/s12567-016-0116-6.
[38] Y. Nakajima, S. Mitani, H. Tani, N. Murakami, T. Yamamoto, K. Yamanaka, Detumbling space debris via thruster plume impingement, in: AIAA/AAS Astrodynamics Specialist Conference, http://dx.doi.org/10.2514/6.2016-5660, arXiv:https://arc.aiaa.org/doi/pdf/10.2514/6.2016-5660. URL https://arc.aiaa.org/doi/abs/10.2514/6.2016-5660.
[39] G. Borelli, G. Gaias, C. Colombo, Rotational Control With Plume Impingement To Aid the Rigid Capture of an Uncooperative Failed Satellite, Adv. Astronaut. Sci. 175 (2021) 4085–4104.
[40] J.-S. Ardaens, G. Gaias, Angles-only relative orbit determination in low earth orbit, Adv. Space Res. 61 (11) (2018) 2740–2760.
[41] J. Ardaens, Angles-only relative navigation in low earth orbit (Ph.D. thesis), TU Delft, 2020.
[42] S. D'Amico, J.-S. Ardaens, G. Gaias, H. Benninghoff, B. Schlepp, J.L. Jørgensen, Noncooperative rendezvous using angles-only optical navigation: System design and flight results, J. Guid. Control Dyn. 36 (6) (2013) 1576–1595, http://dx.doi.org/10.2514/1.59236, arXiv:https://doi.org/10.2514/1.59236.
[43] T. Flohrer, H. Krag, H. Klinkrad, Assessment and categorization of TLE orbit errors for the US SSN catalogue, 2008.
[44] G. Gaias, S. D'Amico, J.-S. Ardaens, Angles-only navigation to a noncooperative satellite using relative orbital elements, J. Guid. Control Dyn. 37 (2) (2014) 439–451, http://dx.doi.org/10.2514/1.61494, arXiv:https://doi.org/10.2514/1.61494.
[45] G. Gaias, S. D'Amico, Impulsive maneuvers for formation reconfiguration using relative orbital elements, J. Guid. Control Dyn. 38 (6) (2015) 1036–1049, http://dx.doi.org/10.2514/1.G000189.
[46] G. Gaias, S. D'Amico, J.-S. Ardaens, Generalised multi-impulsive manoeuvres for optimum spacecraft rendezvous in near-circular orbit, Int. J. Space Sci. Eng. 3 (1) (2015) 68–88.
[47] S. D'Amico, Autonomous formation flying in low earth orbit (Ph.D. thesis), TU Delft, 2010.
[48] G. Gaias, J.-S. Ardaens, O. Montenbruck, Model of J_2 perturbed satellite relative motion with time-varying differential drag, Celestial Mech. Dynam. Astronom. 123 (4) (2015) 411–433, http://dx.doi.org/10.1007/s10569-015-9643-2.
[49] J. Grzymisch, W. Fichter, Observability criteria and unobservable maneuvers for in-orbit bearings-only navigation, J. Guid. Control Dyn. 37 (4) (2014) 1250–1259, http://dx.doi.org/10.2514/1.62476, arXiv:https://doi.org/10.2514/1.62476.
[50] J. Grzymisch, W. Fichter, Analytic optimal observability maneuvers for in-orbit bearings-only rendezvous, J. Guid. Control Dyn. 37 (5) (2014) 1658–1664, http://dx.doi.org/10.2514/1.G000612, arXiv:https://doi.org/10.2514/1.G000612.
[51] G. Gaias, M. Lovera, Trajectory design for proximity operations: The relative orbital elements' perspective, J. Guid. Control Dyn. 44 (12) (2021) 2294–2302, http://dx.doi.org/10.2514/1.G006175, arXiv:https://doi.org/10.2514/1.G006175.
[52] G. Gaias, C. Colombo, M. Lara, Analytical framework for precise relative motion in low earth orbits, J. Guid. Control Dyn. 43 (5) (2020) 915–927, http://dx.doi.org/10.2514/1.G004716, arXiv:https://doi.org/10.2514/1.G004716.
[53] G. Gaias, J.-S. Ardaens, Design challenges and safety concept for the AVANTI experiment, Acta Astronaut. 123 (2016) 409–419, http://dx.doi.org/10.1016/j.actaastro.2015.12.034, special Section: Selected Papers from the International Workshop on Satellite Constellations and Formation Flying 2015. URL https://www.sciencedirect.com/science/article/pii/S0094576515004737.
[54] W. Fehse, Automated Rendezvous and Docking of Spacecraft, in: Cambridge Aerospace Series, Cambridge University Press, 2003, http://dx.doi.org/10.1017/CBO9780511543388.